Journal of Energy Chemistry 69 (2022) 348–355

Contents lists available at ScienceDirect

Journal of Energy Chemistry

journal homepage: www.elsevier.com/locate/jechem

http://www.journals.elsevier.com/journal-of-energy-chemistry/

Self-template-oriented synthesis of lead-free perovskite $Cs_3Bi_2I_9$ nanosheets for boosting photocatalysis of CO_2 reduction over Z-scheme heterojunction $Cs_3Bi_2I_9/CeO_2$

You-Xiang Feng [a], Guang-Xing Dong [a], Ke Su [a], Zhao-Lei Liu [a], Wen Zhang [a,*], Min Zhang [a,b,*], Tong-Bu Lu [a]

[a] MOE International Joint Laboratory of Materials Microstructure, Institute for New Energy Materials and Low Carbon Technologies, School of Materials Science and Engineering, Tianjin University of Technology, Tianjin 300384, China
[b] Tianjin Key Laboratory of Organic Solar Cells and Photochemical Conversion, School of Chemistry and Chemical Engineering, Tianjin University of Technology, Tianjin 300384, China

ARTICLE INFO

Article history:
Received 10 November 2021
Revised 31 December 2021
Accepted 9 January 2022
Available online 19 January 2022

Keywords:
Lead-free perovskite
Z-scheme heterojunction
$Cs_3Bi_2I_9$ nanosheets
Photocatalytic CO_2 reduction
H_2O oxidation

ABSTRACT

Lead halide perovskite (LHP) nanocrystals have been intensely studied as photocatalysts for artificial photosynthesis in recent years. However, the toxicity of lead in LHP seriously limits their potential for widespread applications. Herein, we first present the synthesis of 2D lead-free halide perovskite ($Cs_3Bi_2I_9$) nanosheets with self-template-oriented method, in which $BiOI/Bi_2O_{2.7}$ nanosheets were used as the template and Bi ion source simultaneously. Through facile electrostatic self-assembly strategy, a Z-scheme heterojunction composed of $Cs_3Bi_2I_9$ nanosheets and CeO_2 nanosheets ($Cs_3Bi_2I_9/CeO_2$-3:1) was constructed as photocatalyst for the photo-reduction of CO_2 coupled with the oxidation of H_2O. Due to the matching energy levels and the close interfacial contact between $Cs_3Bi_2I_9$ and CeO_2 nanosheets, the separation efficiency of the photogenerated carriers in $Cs_3Bi_2I_9/CeO_2$-3:1 composite was significantly improved. Consequently, the environment-friendly halide perovskite heterojunction $Cs_3Bi_2I_9/CeO_2$-3:1 presents impressive photocatalytic activity for the reduction of CO_2 to CH_4 and CO with an electron consumption yield of 877.04 μmol g^{-1}, which is over 7 and 15 times higher than those of pristine $Cs_3Bi_2I_9$ and CeO_2 nanosheets, exceeding the yield of other reported bismuth-based perovskite for photocatalytic CO_2 reduction.

© 2021 Science Press and Dalian Institute of Chemical Physics, Chinese Academy of Sciences. Published by ELSEVIER B.V. and Science Press. All rights reserved.

1. Introduction

Direct utilization of solar energy to convert CO_2 into energy-rich compounds is expected to provide a solution to alleviate climate and energy crisis [1–6]. To push this ideal energy conversion technology toward practical applications, photocatalytic reduction of CO_2 integrated with the oxidation of H_2O was considered as a prospective approach to support the sustainable energy needs [7–8]. In this context, many semiconductors (e.g., TiO_2 [9,10], $CsPbBr_3$ [11], Cu_2O [12,13], BiOBr [14] etc.) have been explored as photoactive materials for artificial photosynthesis. Among them, lead-based halide perovskite (LHP) nanocrystals are considered as promising photocatalysts [11,15–20], due to their fascinating light-harvesting performance, long photogenerated carrier lifetime and low-cost characteristics [21–23]. However, the proverbial toxicity of lead to human life, because of its well solubility in water, limits their future widespread applications.

As alternatives, nontoxic elements such as Sn, Sb, and Bi have recently received extensive considerations in the preparation of lead-free halide perovskites [24–27]. Nevertheless, compared to the Pb-based perovskites, the homovalent Sn^{2+}-based perovskites were either unstable or less efficient [28]. While for the heterovalent Sb and Bi ions [29,30], these two elements have the same stable +3 oxidation state and are less toxic in comparison with Pb. Particularly, Bi^{3+} has the similar electron configuration and ion radius with Pb^{2+}, which may bring about analogous optoelectronic characteristics as LHP. In this respect, the Bi-based perovskites, especially $Cs_3Bi_2X_9$ (X = Cl, Br or I) perovskites, have been widely employed in photocatalytic applications such as H_2O decomposition [31,32], organic reactions [33,34], pollutant degradations [35], and CO_2 reduction [36–38].

Nevertheless, as photoactive catalysts, the primary concerns of $Cs_3Bi_2X_9$ perovskites are the defect characteristics of these materials [39]. As the low formation energy, many deep energy defects

---

* Corresponding authors.
E-mail addresses: zhangwen@email.tjut.edu.cn (W. Zhang), zm2016@email.tjut.edu.cn (M. Zhang).

https://doi.org/10.1016/j.jechem.2022.01.015
2095-4956/© 2021 Science Press and Dalian Institute of Chemical Physics, Chinese Academy of Sciences. Published by ELSEVIER B.V. and Science Press. All rights reserved.

exist in the band gap of $Cs_3Bi_2X_9$, which would become the recombination centers of photogenerated carriers [39]. Besides, the high exciton binding energy in $Cs_3Bi_2X_9$ further hampers the separation of the photogenerated electrons and holes in $Cs_3Bi_2X_9$. Aimed at above problems, the structures and compositions of Bi-based halide perovskite catalysts have been modulated with various strategies over the past 3 year, such as doping $Cs_3Bi_2X_9$ with random morphologies on C_3N_4 [40], TiO_2 [41] and Bi_2WO_6 [38], or adjusting the cations [42,43] or halide constitutes [36,44] of Bi-based halide perovskite nanocrystals. Nonetheless, the performance of Bi-based halide perovskites for CO_2 reduction is still far from satisfactory. Previous reports have demonstrated that compared with traditional metal halide perovskite nanocrystals, 2D perovskite nanosheets possess prior stability [45], abundant active sites [46], and shorter carriers transfer distance to the surface of photocatalysts [47,48]. Therefore, it is highly anticipated to synthesis 2D Bi-based halide perovskite nanostructure, which has not been reported yet, and employed it as the photoactive material for the construction of heterojunction catalysts to promote the performance of Bi-based perovskite for CO_2 photo-reduction.

In this work, using $BiOI/Bi_2O_{2.7}$ nanosheets as both template and Bi ion source, we first present a self-template-oriented method for the synthesis of 2D lead-free halide perovskite ($Cs_3Bi_2I_9$) nanosheets. To further improve the carrier dissociation of 2D $Cs_3Bi_2I_9$ nanosheets, 2D CeO_2 nanosheets, which possess high oxidation capacity, stability and low-cost properties, are committed to constructing a Z-scheme heterojunction ($Cs_3Bi_2I_9/CeO_2$-3:1) through facile electrostatic self-assembly between $Cs_3Bi_2I_9$ and CeO_2 nanosheets (Scheme 1). Specifically, the construction of 2D $Cs_3Bi_2I_9$ nanosheets-based Z-scheme heterojunctions as photocatalysts is based on the following important considerations. Firstly, 2D/2D heterojunction has large contact area, rich charge transfer channels, and shortened charge transfer distance, which is conducive to the effective transfer and separation of photogenerated carriers. Secondly, Z-scheme heterojunction could maintain the redox capacity of each component [49]. Consequently, the environment-friendly perovskite heterojunction $Cs_3Bi_2I_9/CeO_2$-3:1 shows outstanding activity for the reduction of CO_2 coupled with the oxidation of H_2O, demonstrating a record activity of 238.21 μmol g^{-1} and a highest electron consumption yield of 877.04 μmol g^{-1} among the reported bismuth-based perovskite photocatalysts.

2. Experimental

2.1. Synthesis of $Cs_3Bi_2I_9$ nanosheets

$Cs_3Bi_2I_9$ nanosheets were synthesized by self-template-oriented method using $BiOI/Bi_2O_{2.7}$ nanosheets, which have been synthesized by solvothermal method according to the previous report [50], as template and Bi ion source simultaneously. Firstly, CsI (100 mg, 0.38 mmol) was added into the mixture solution of isopropyl alcohol (IPA, 10 mL), hydroiodic acid (HI, 0/60 μL) and ethyl alcohol (1 mL) and stirred until evenly dispersed. Then, 50 mg $BiOI/Bi_2O_{2.7}$ nanosheets were dispersed into above system at room temperature and stirred for 12 h. The resulting $Cs_3Bi_2I_9$ nanosheets were collected by centrifugation and washed with IPA to remove residual ions.

2.2. Synthesis of $Cs_3Bi_2I_9/CeO_2$ heterojunction photocatalysts

The $Cs_3Bi_2I_9/CeO_2$ heterojunction was constructed via electrostatic assembly strategy. Specifically, the total mass of $Cs_3Bi_2I_9$ and CeO_2 nanosheets was fixed at 20 mg, and the ratio of the two nanosheets ranged from 2:1 to 6:1. Subsequently, the two components were fully dispersed in *n*-hexane (5 mL) by ultrasonic and continuous stirring. After the evaporation of *n*-hexane at 50 °C, $Cs_3Bi_2I_9/CeO_2$-x:1 (x = 2–6) assembly can be obtained.

3. Results and discussion

3.1. Self-template-oriented synthesis of $Cs_3Bi_2I_9$ nanosheets

Firstly, the structure and morphology of $BiOI/Bi_2O_{2.7}$ nanosheets were characterized by powder X-ray diffraction (PXRD), transmission electron microscope (TEM), atomic force microscope (AFM)

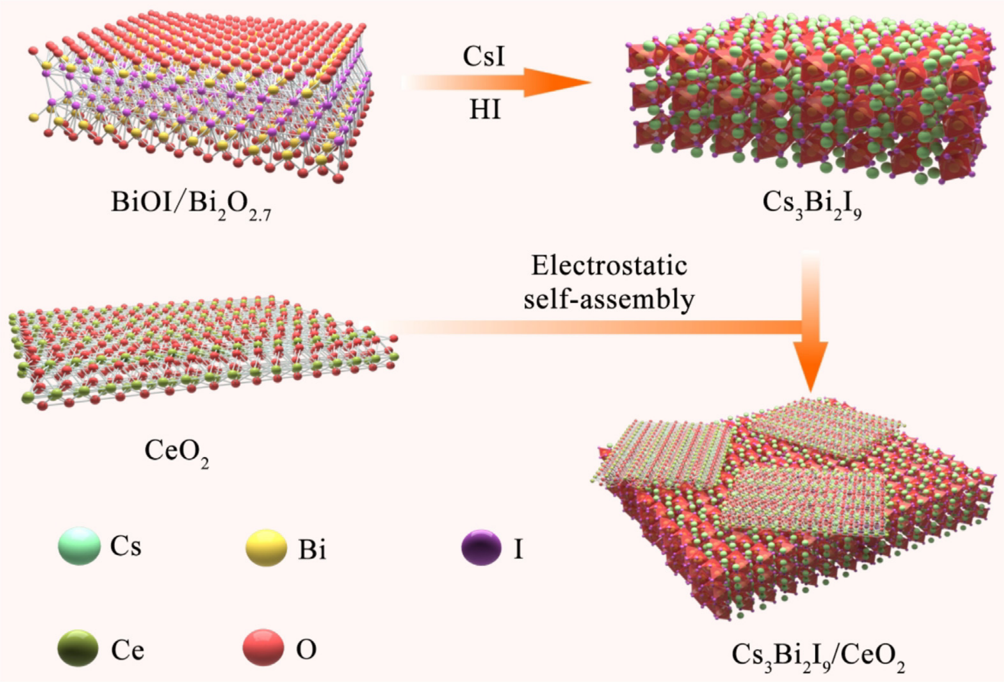

Scheme 1. The preparation of $Cs_3Bi_2I_9$ nanosheets and the self-assembly between $Cs_3Bi_2I_9$ and CeO_2 nanosheets.

and elemental mapping measurements (Fig. S1, Fig. S2, and Fig. 1). The PXRD pattern in Fig. S1 shows that a mixture of two phases: tetragonal BiOI (JCPDS: 10-0445) and tetragonal $Bi_2O_{2.7}$ (JCPDS: 75-0993) coexist in the spectrum. Typical TEM and AFM measurements (Fig. 1a and b) show that $BiOI/Bi_2O_{2.7}$ nanosheets exhibit a lateral dimension of 50–100 nm and a thickness of around 6.0 nm. As the template and Bi^{3+} source, the $BiOI/Bi_2O_{2.7}$ nanosheets were subsequently added into the mixed solution of isopropyl alcohol/ethyl alcohol (*V*:*V*, 10:1) together with CsI and HI (see details in the Experimental Section). The transformation of $BiOI/Bi_2O_{2.7}$ to $Cs_3Bi_2I_9$ was tracked by XRD spectra measurements. As shown in Fig. 1(c), within the same reaction conditions, the system with HI can convert $BiOI/Bi_2O_{2.7}$ to $Cs_3Bi_2I_9$ more thoroughly than the system without HI. Such phenomenon was speculated to the gradually corrosion of HI to $BiOI/Bi_2O_{2.7}$, which would promote the release of Bi^{3+} ions source and act as the template in situ for the formation of $Cs_3Bi_2I_9$ [51]. The UV–vis diffuse reflectance spectra (DRS, Fig. S3) show that, in comparison with $BiOI/Bi_2O_{2.7}$, $Cs_3Bi_2I_9$ shows a red-shifted absorption band and displays an excitonic transition centered at 495 nm [42].

In addition, the TEM image (Fig. 1d) shows that the obtained $Cs_3Bi_2I_9$ samples are also 2D nanosheets, and the thickness of $Cs_3Bi_2I_9$ nanosheets measured by AFM (Fig. S4) is 6–8 nm, which is similar to that of $BiOI/Bi_2O_{2.7}$ nanosheets, suggesting that in the transformation process of $BiOI/Bi_2O_{2.7}$ to $Cs_3Bi_2I_9$, $BiOI/Bi_2O_{2.7}$ could act as both template and Bi ions source simultaneously and the morphology of $BiOI/Bi_2O_{2.7}$ precursors was maintained. In addition, the subtle nanostructure and composition of $Cs_3Bi_2I_9$ nanosheets were further characterized by the high-resolution TEM (HRTEM) and elemental mapping measurements. As shown in Fig. 1(e), the lattice spacing of 0.42 nm corresponds to the (110) crystal plane of $Cs_3Bi_2I_9$, and the elemental mapping images in Fig. 1(f–h) demonstrate the uniform distribution of Cs, Bi and I elements. These results clearly suggest that $Cs_3Bi_2I_9$ nanosheets were successfully synthesized with the self-template-oriented strategy.

3.2. The construction of $Cs_3Bi_2I_9/CeO_2$ heterojunction via electrostatic assembly

To construct 2D/2D heterojunction $Cs_3Bi_2I_9/CeO_2$, 2D CeO_2 nanosheets were synthesized using the modified procedures of previous report (see supporting information file for detail) [52]. The PXRD measurement (Fig. S5) demonstrates the face-centered cubic crystalline structure of CeO_2 (JCPDS 34-0394). The TEM test shows that the transverse size of the prepared CeO_2 nanosheets is 20–30 nm (Fig. 1i), and the thickness is estimated to be 1.5 nm through AFM measurement (Fig. S6). Additionally, the elemental mapping images of CeO_2 nanosheets demonstrate that the Cs and O elements are uniformly dispersed in the nanosheets (Fig. S7). All these results indicate the successful preparation of CeO_2 nanosheets. Right after the synthesis of these two 2D materials, the possibility of electrostatic assembly between $Cs_3Bi_2I_9$ and CeO_2 nanosheets was evaluated. The Zeta potentials of as-prepared $Cs_3Bi_2I_9$ and CeO_2 nanosheets were tested in isopropanol. The results in Fig. 2(a) show that the Zeta potentials of $Cs_3Bi_2I_9$ and CeO_2 nanosheets are measured as −59.87 and 25.37 mV, respectively. The reversed polarity offers the potential of electrostatic assembly between the negatively charged $Cs_3Bi_2I_9$ nanosheets and the positively charged CeO_2 nanosheets.

Subsequently, the $Cs_3Bi_2I_9/CeO_2$-*x*:1 (*x* = 2–6) assemblies were prepared by fully mixing $Cs_3Bi_2I_9$ nanosheets with different amounts of CeO_2 nanosheets (mass ratio of $Cs_3Bi_2I_9$:CeO_2 = 2/3/4/5/6:1) under ultrasonic conditions. The structure and morphology of $Cs_3Bi_2I_9/CeO_2$-*x*:1 were analyzed by the PXRD, FTIR, UV–vis DRS and TEM measurements. The PXRD patterns in Fig. 2(b) indicate that there are diffraction peaks of both $Cs_3Bi_2I_9$ and CeO_2 in $Cs_3Bi_2I_9/CeO_2$-*x*:1 composites. As the amount of $Cs_3Bi_2I_9$ increases, the relative diffraction intensity of $Cs_3Bi_2I_9$ gradually increases, suggesting the successful assembly of $Cs_3Bi_2I_9$ and CeO_2 nanosheets. Besides, the FTIR results in Fig. S8 show that the characteristic peaks of CeO_2 (black line, 1629 cm^{-1} and 551 cm^{-1}) and $Cs_3Bi_2I_9$ (red line, 1646 cm^{-1}, 1406 cm^{-1},

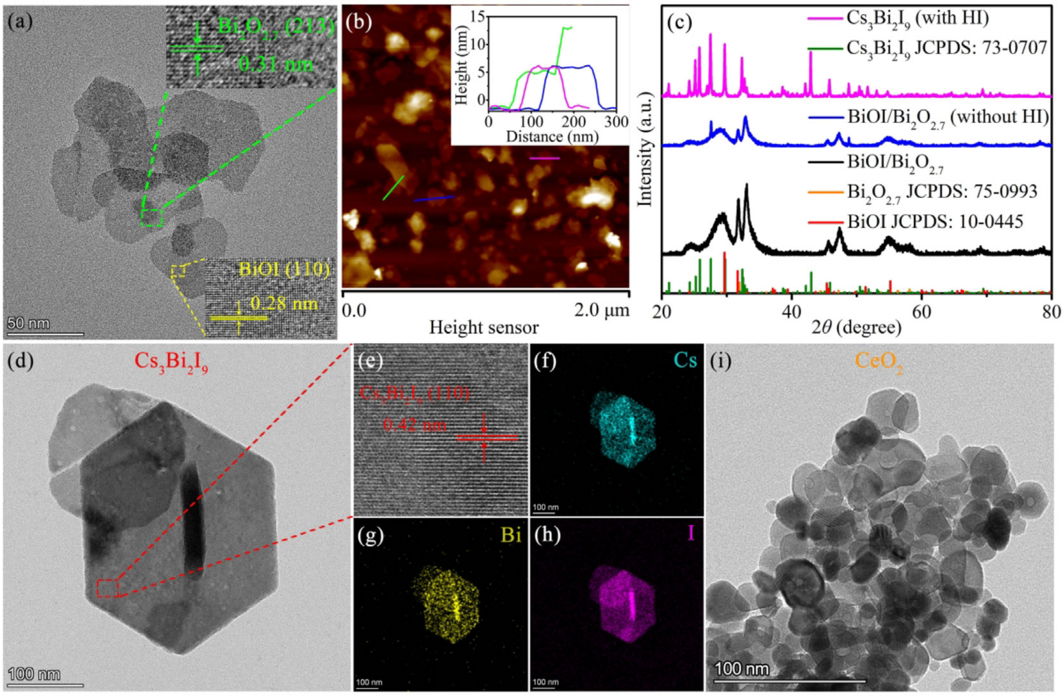

Fig. 1. (a) TEM and (b) AFM images of $BiOI/Bi_2O_{2.7}$ nanosheets. (c) XRD patterns of $BiOI/Bi_2O_{2.7}$ and samples transformed from $BiOI/Bi_2O_{2.7}$ to $Cs_3Bi_2I_9$ in the absence/presence of HI. (d) TEM image of $Cs_3Bi_2I_9$ nanosheets. (e) HRTEM image and (f–h) elemental mapping images of $Cs_3Bi_2I_9$ nanosheets. (i) TEM image of CeO_2 nanosheets.

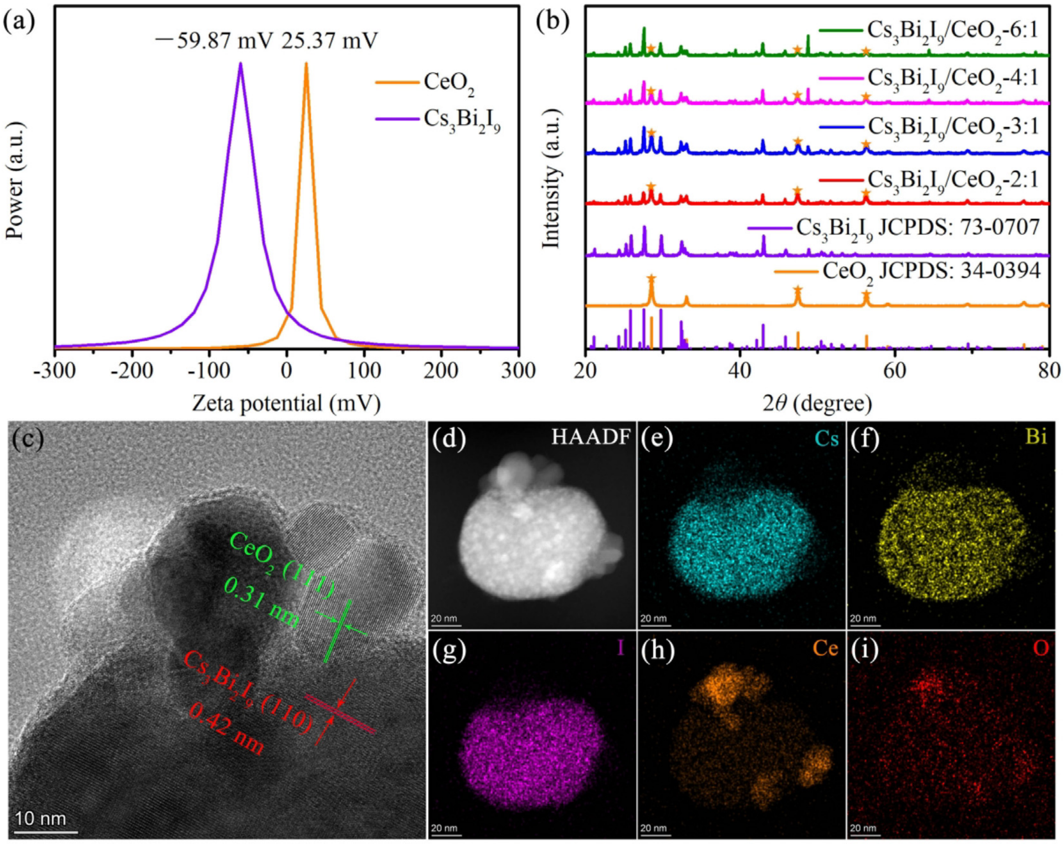

Fig. 2. (a) Zeta potentials of $Cs_3Bi_2I_9$ and CeO_2. (b) XRD patterns of $Cs_3Bi_2I_9$, CeO_2 and $Cs_3Bi_2I_9/CeO_2$-x:1 (x = 2–6) assemblies. (c) HRTEM image of $Cs_3Bi_2I_9/CeO_2$-3:1 assembly. (d-i) HAADF image and elemental mapping images of $Cs_3Bi_2I_9/CeO_2$-3:1.

1283 cm^{-1} and 1114 cm^{-1}) coexist in the $Cs_3Bi_2I_9/CeO_2$-3:1 composite, indicating $Cs_3Bi_2I_9$ nanosheets and CeO_2 nanosheets were assembled together through electrostatic interactions. Further, the UV–vis DRS of CeO_2, $Cs_3Bi_2I_9$ and $Cs_3Bi_2I_9/CeO_2$-x:1 in Fig. S9 show that $Cs_3Bi_2I_9/CeO_2$-x:1 assemblies have wide visible light absorption range (up to 670 nm) and enhanced light absorption below 370 nm with the increase of CeO_2 contents, suggesting the electrostatic assembly between $Cs_3Bi_2I_9$ and CeO_2 nanosheets can retain their absorption ability to UV–vis light spectrum. To further explore the subtle nanostructure of $Cs_3Bi_2I_9/CeO_2$-x:1, HRTEM measurements were conducted on $Cs_3Bi_2I_9/CeO_2$-3:1 sample. As shown in Fig. 2(c), CeO_2 nanosheets stacked on the edge of $Cs_3Bi_2I_9$ nanosheets. The lattice spacings of 0.31 nm and 0.42 nm are ascribed to the (111) crystalline plane of CeO_2 nanosheets and the (110) crystalline plane of $Cs_3Bi_2I_9$ nanosheets, respectively. Further, the assembly behavior of $Cs_3Bi_2I_9$ and CeO_2 nanosheets was also confirmed by the corresponding HAADF image and elemental mapping images (Fig. 2d–i), demonstrating the close contact of $Cs_3Bi_2I_9$ and CeO_2 nanosheets in the $Cs_3Bi_2I_9/CeO_2$-3:1 assembly.

3.3. Band structures of $Cs_3Bi_2I_9/CeO_2$ heterojunction

To further obtain the redox thermodynamic data of $Cs_3Bi_2I_9$ and CeO_2 nanosheets, we calculated the band gaps of $Cs_3Bi_2I_9$ and CeO_2 from their Tauc plots (Fig. S10a–S10b). Additionally, the conduction band (CB) potentials of $Cs_3Bi_2I_9$ and CeO_2 nanosheets were determined by Mott–Schottky plots measurements (Fig. S10c–S10d). As shown in Fig. S10, the band gaps of $Cs_3Bi_2I_9$ and CeO_2 nanosheets were measured as 1.90 eV and 2.82 eV, respectively. As the Mott–Schottky plots of both $Cs_3Bi_2I_9$ and CeO_2 have positive slopes, confirming the n-type semiconductor behavior of $Cs_3Bi_2I_9$ and CeO_2. The CB potentials of $Cs_3Bi_2I_9$ and CeO_2 nanosheets were valued as −0.97 V and −0.69 V (vs NHE), respectively. Accordingly, the valence band (VB) potentials of $Cs_3Bi_2I_9$ and CeO_2 nanosheets can be calculated as 0.93 V and 2.13 V (vs NHE) respectively. In combination with above results, the relative energy-band alignments of $Cs_3Bi_2I_9$ and CeO_2 nanosheets can be illustrated in Fig. 3 (a), demonstrating a staggered band structure configuration.

It is well known that, for heterojunction catalysts, interfacial charge transfer direction plays an important role for their photoactivities. Therefore, the X-ray photoelectron spectroscopy (XPS) measurements of $Cs_3Bi_2I_9$, CeO_2, and $Cs_3Bi_2I_9/CeO_2$-3:1 assembly were carried out. As displayed in Fig. 3(b), the Ce 3d peak of CeO_2 displays eight peaks at 916.70, 907.60, 902.70, 900.80, 898.30, 888.90, 884.60 and 882.15 eV, which can be attributed to Ce 3$d_{5/2}$ and Ce 3$d_{3/2}$ respectively [53]. In comparison with the pristine CeO_2 sample, the binding energies of Ce 3d peaks in $Cs_3Bi_2I_9/CeO_2$-3:1 present obvious negative shifts (0.15 eV ~ 0.30 eV). Similarly, the bonding energies of O 1s peaks (531.30 eV and 529.10 eV) in $Cs_3Bi_2I_9/CeO_2$-3:1 also show significant negative shifts (0.33 eV ~ 0.39 eV) with respect to those of pure CeO_2 (Fig. 3c), indicating the increase of electron density on CeO_2 after being assembled with $Cs_3Bi_2I_9$. On the other hand, the binding energy of Bi 4f shows two characteristic peaks at 158.90 eV and 164.20 eV, assigning to the Bi 4$f_{7/2}$ and Bi 4$f_{5/2}$, respectively. Compared with individual $Cs_3Bi_2I_9$, the binding energies of Bi 4f peaks in $Cs_3Bi_2I_9/CeO_2$-3:1 assembly display obvious shifts to higher energy by ~0.2 eV (Fig. 3d) [54]. These significant binding energy shifts of Ce, O and Bi demonstrate that the electrostatic assembly between $Cs_3Bi_2I_9$ and CeO_2 could bring about the interfacial electron transfer from $Cs_3Bi_2I_9$ to CeO_2, leading to an internal electric

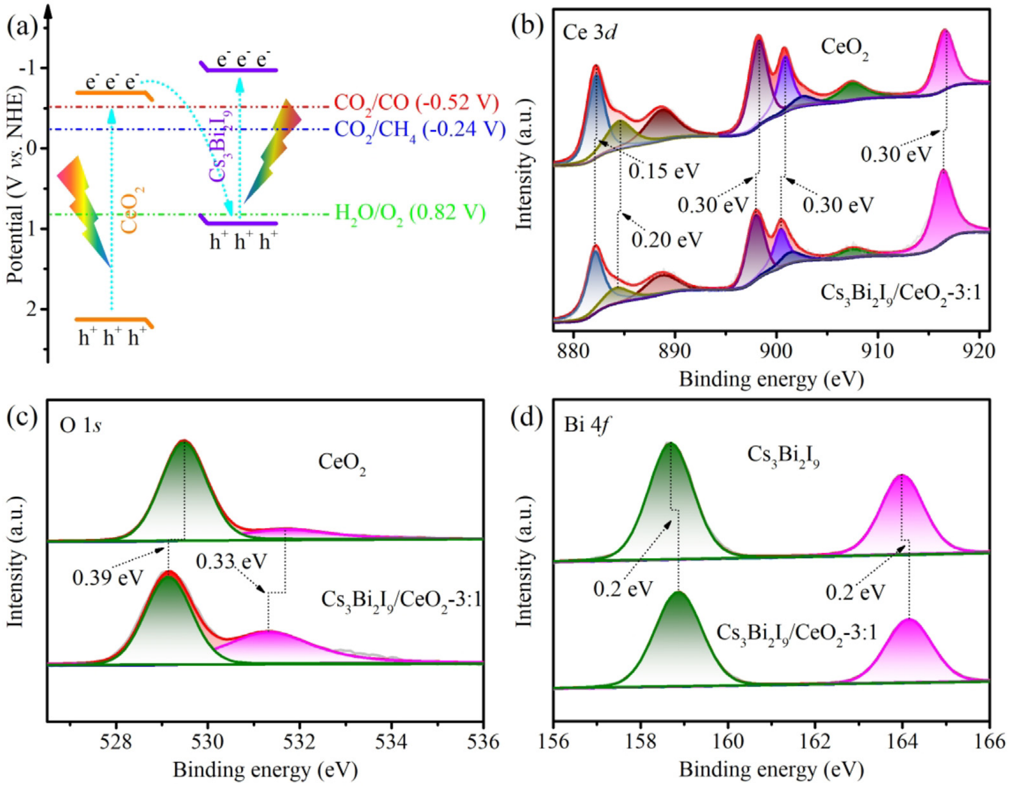

Fig. 3. (a) Band structures of $Cs_3Bi_2I_9$ and CeO_2. High-resolution XPS spectra of (b) Ce 3*d* and (c) O 1*s* for CeO_2 and $Cs_3Bi_2I_9/CeO_2$-3:1, (d) Bi 4*f* for $Cs_3Bi_2I_9$ and $Cs_3Bi_2I_9/CeO_2$-3:1.

field with the orientation from $Cs_3Bi_2I_9$ to CeO_2, which would facilitate the transfer of the photogenerated electrons from CeO_2 to $Cs_3Bi_2I_9$ [55]. Combining with the staggered band structure of $Cs_3Bi_2I_9$ and CeO_2 in Fig. 3(a), the transfer of photogenerated carriers in $Cs_3Bi_2I_9/CeO_2$-3:1 assembly tends to comply with the type of Z-scheme heterojunction.

3.4. Photocatalytic CO_2 reduction

Encouraged by the positive results above, the photocatalytic performance of $Cs_3Bi_2I_9/CeO_2$-*x*:1 for CO_2 reduction coupled with H_2O oxidation was assessed. Here, we conducted the photoreaction in a gas–solid reactor, in which CO_2 gas and water vapor were injected simultaneously as reactants and irradiated with 300 W Xe lamp. The results in Fig. 4(a) and Fig. S11 show that for pure $Cs_3Bi_2I_9$ and CeO_2 catalytic systems, the main product in the gas phase is CO, with the yield of 62.43 μmol g^{-1} and 28.22 μmol g^{-1}, respectively. The corresponding electron reduction yields in these systems are only 124.86 μmol g^{-1} and 56.44 μmol g^{-1}, respectively. Under the same reaction conditions, the $Cs_3Bi_2I_9/CeO_2$-*x*:1 assemblies present significantly elevated performance for CO_2 reduction. As shown in Fig. 4(a), the product yields of $Cs_3Bi_2I_9/CeO_2$-*x*:1 with various compositions are all higher than those of independent components. Meanwhile, the ratio between $Cs_3Bi_2I_9$ and CeO_2 nanosheets has a significant impact on the photocatalytic performance of the assembly. The highest reaction activity is achieved by $Cs_3Bi_2I_9/CeO_2$-3:1 assembly. The total yield of reduction products, including CO and CH_4, reaches 238.21 μmol g^{-1} and the electron consumption yield is calculated as 877.04 μmol g^{-1}, which is over 7 and 15 times higher than those of pristine $Cs_3Bi_2I_9$ and CeO_2 nanosheets, demonstrating a record yield among the reported bismuth-based perovskite for photocatalytic CO_2 reduction (Table S1, Fig. 4b). Here, the catalytic activity of the assembly decreases obviously when the ratio of $Cs_3Bi_2I_9$ to CeO_2 is larger than 3:1, indicating that the appropriate ratio of $Cs_3Bi_2I_9$ to CeO_2 is critical to improve the catalytic activity of the assembly. Additionally, the evolution of O_2 has also been quantified. As shown in Fig. S12, the amount of oxygen generated using $Cs_3Bi_2I_9/CeO_2$-3:1 is 208.86 μmol g^{-1}, thus the ratio of electron and hole consumption in this photoredox reaction is close to 1. This result suggests that the reduction and oxidation reactions are basically in balance. In order to explore the advantages of self-template-oriented method for the synthesis of $Cs_3Bi_2I_9$ nanosheets as photocatalysts, $Cs_3Bi_2I_9$ nanocrystals ($Cs_3Bi_2I_9$ NCs) were prepared by hot injection method [56] and characterized by XRD and TEM measurements (Fig. S13). Additionally, the prepared $Cs_3Bi_2I_9$ NCs and $Cs_3Bi_2I_9$ NCs/CeO_2 samples were tested as photocatalysts for the reduction of CO_2. The results in Fig. S14 show that in comparison with the samples synthesized by self-template-oriented method, $Cs_3Bi_2I_9$ NCs and $Cs_3Bi_2I_9$ NCs/CeO_2 demonstrate only one-eighth and one-eighteenth production of $Cs_3Bi_2I_9$ nanosheets and $Cs_3Bi_2I_9/CeO_2$-3:1, respectively. These results demonstrate that the 2D $Cs_3Bi_2I_9$ nanosheets synthesized by self-template-oriented method have obvious advantages as photocatalysts. Further control experiments in Fig. S15 demonstrate that in the absence of CO_2, H_2O, light source, or $Cs_3Bi_2I_9/CeO_2$-3:1 assembly, few reduction products can be detected, suggesting all these elements are indispensable for the significant generation of CO and CH_4. Notably, the origin of a small amount of CO produced in Ar/H_2O and CO_2/catalyst conditions was speculated to the partial decomposition of surface ligands (polyvinylpyrrolidone and alcohols), which were confirmed by the characteristic stretching vibrations signal of C–N and C–O on the infrared spectrum (Fig. S8).

To further illustrate the origin of CO and CH_4 products, the isotope tracking experiment using $^{13}CO_2$ as carbon resource was carried out. The result in Fig. 4(c) (bottom) shows that the *m*/*z* value of

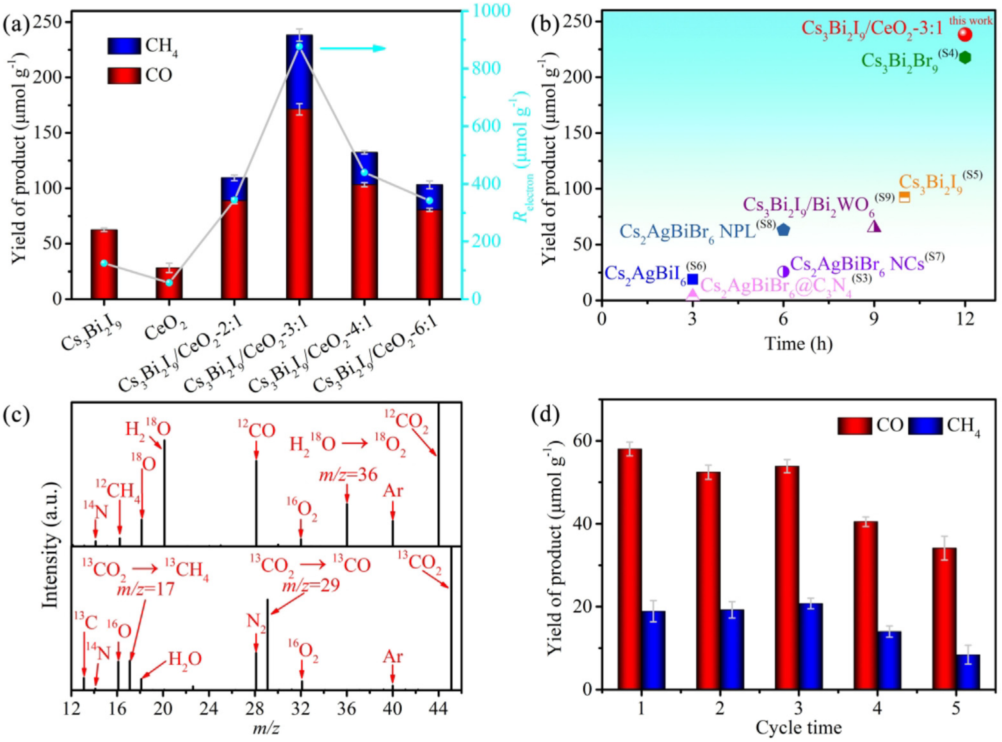

Fig. 4. (a) The yields of CO and CH_4 over $Cs_3Bi_2I_9$, CeO_2 and $Cs_3Bi_2I_9/CeO_2$-x:1 (x = 2–6) in 12 h. (b) Comparative data of $Cs_3Bi_2I_9/CeO_2$-3:1 for CO_2 reduction with other bismuth-based perovskites. (c) MS spectra of $^{13}CO_2$ (bottom) and $H_2^{18}O$ (top) isotope experiments in $Cs_3Bi_2I_9/CeO_2$-3:1 photocatalytic system. (d) Recycling experiments of $Cs_3Bi_2I_9/CeO_2$-3:1 catalyst with five cycles (4 h/cycle).

17 and 29, belonging to the peak of $^{13}CH_4$ and ^{13}CO, can be clearly detected, confirming that CO and CH_4 products are mainly generated from the reduction of CO_2 instead of the decomposition of other organic substrates. In addition, the oxidation of H_2O was also investigated by the isotope trace experiment using $H_2^{18}O$ instead of H_2O. The mass spectrometry result (Fig. 4c, top) indicates that oxidation product $^{18}O_2$ can be obtained, demonstrating that water oxidation supplied the electrons in this photocatalytic system. In addition, the stability of $Cs_3Bi_2I_9/CeO_2$-3:1 photocatalyst was evaluated by recycling experiments. As shown in Fig. 4(d), after three consecutive cycles, there is no obvious deactivation of CO and CH_4 production. While after the fourth and the fifth recycling experiments, the activity of $Cs_3Bi_2I_9/CeO_2$-3:1 reduced to 71% and 55% of the initial state, respectively, suggesting that in a certain period of time (12 h), the catalyst can maintain relative stability. Moreover, the comparative PXRD and XPS measurements of $Cs_3Bi_2I_9/CeO_2$-3:1 before and after photoreaction (12 h, Fig. S16, Fig. S17) indicate that no significant crystalline changes were observed for both $Cs_3Bi_2I_9$ and CeO_2. In addition, we conducted a photocatalytic CO_2 conversion tracking experiment on $Cs_3Bi_2I_9/CeO_2$-3:1 assembly (Fig. S18). The evolution of CO and CH_4 shows a linear increase within 12 h of illumination. These results together indicate that $Cs_3Bi_2I_9/CeO_2$-3:1 assembly is relatively stable during this photoredox experiment.

3.5. Photocatalytic mechanism analysis

To better understand the photocatalytic mechanism of $Cs_3Bi_2I_9/CeO_2$-3:1 assembly, the in situ irradiated XPS measurements were conducted. As shown in Fig. 5(a and b), in the dark conditions, the Ce 3*d* spectrum of $Cs_3Bi_2I_9/CeO_2$-3:1 displays eight typical peaks at 916.40, 907.60, 901.50, 900.60 eV and 898.00, 888.80, 884.4, 882.30 eV, assigning to the Ce $3d_{3/2}$ and Ce $3d_{5/2}$, respectively. Besides, O 1 *s* spectrum of $Cs_3Bi_2I_9/CeO_2$-3:1 exhibits two characteristic peaks at 531.30 eV, and 529.10 eV (Fig. 5b). Under light irradiation, the binding energies of Ce 3*d* and O 1*s* exhibit distinct positive shifts (0.1–0.29 eV), suggesting a decrease of electron density around Ce and O atoms. Meanwhile, two peaks at 158.87 eV and 164.17 eV for the Bi 4*f* (Fig. 5c) can be clearly identified in $Cs_3Bi_2I_9/CeO_2$-3:1 under dark. Upon light irradiation, two new peaks at the lower binding energies (156.80 eV and 162.10 eV) appeared, which may be related to the formation of metallic Bi (Bi^0) [57]. Such results indicate that under the irradiation of light, the photogenerated electrons transfer from CeO_2 to $Cs_3Bi_2I_9$ and accumulate around Bi atoms, which is in accordance with the Z-scheme heterojunction mechanism mentioned above.

Furthermore, the photogenerated electron transfer pathway in $Cs_3Bi_2I_9/CeO_2$-3:1 assembly was further estimated by electron spin resonance (ESR) detection. Here, 5,5-dimethyl-1-pyrroline-N-oxide (DMPO) was used as a radical trap, which can form stable adducts with hydroxyl radical (•OH). The results in Fig. 5(d) show that under light conditions, the characteristic peaks of DMPO-•OH were detected in the presence of CeO_2 or $Cs_3Bi_2I_9/CeO_2$-3:1, while $Cs_3Bi_2I_9$ alone could not produce hydroxyl radicals. The reason is ascribed to the less positive VB potential of $Cs_3Bi_2I_9$ (0.93 V vs. NHE), which is higher than the oxidation potential of H_2O/.OH (1.99 V vs. NHE) [58]. This result suggests that the oxidation of H_2O can only occur on CeO_2, and in comparison with the individual CeO_2, $Cs_3Bi_2I_9/CeO_2$-3:1 assembly displays much higher intensity of DMPO-.OH, indicating the higher activity of $Cs_3Bi_2I_9/CeO_2$-3:1 for H_2O oxidation. In combination with the ISI-XPS results that the photogenerated electron can transfer from CeO_2 to $Cs_3Bi_2I_9$ in $Cs_3Bi_2I_9/CeO_2$-3:1 assembly, the Z-scheme heterojunction mechanism can be further documented. That is, under light conditions, photogenerated carriers are generated in $Cs_3Bi_2I_9/CeO_2$-3:1 assembly; on the one hand, the photogenerated electrons transfer from

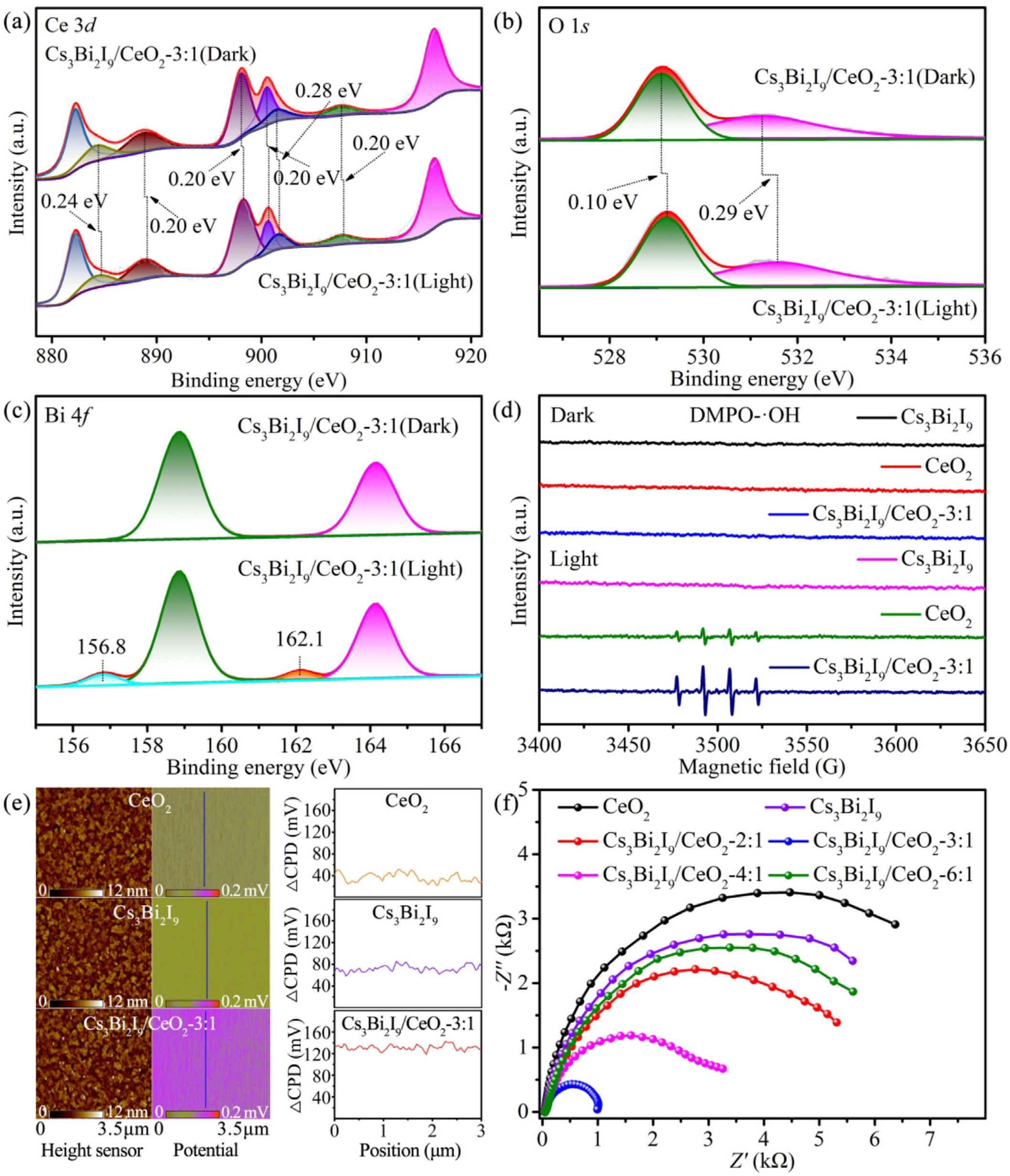

Fig. 5. High-resolution XPS spectra of (a) Ce 3*d*, (b) O 1*s* and (c) Bi 4*f* for $Cs_3Bi_2I_9/CeO_2$-3:1 under dark and light conditions. (d) ESR spectra of $Cs_3Bi_2I_9$, CeO_2 and $Cs_3Bi_2I_9/CeO_2$-3:1 using DMPO as a radical trap. (e) KPFM measurements of $Cs_3Bi_2I_9$, CeO_2 and $Cs_3Bi_2I_9/CeO_2$-3:1. (f) EIS Nyquist plots of $Cs_3Bi_2I_9$, CeO_2 and $Cs_3Bi_2I_9/CeO_2$-*x*:1 (*x* = 2–6).

CeO_2 to $Cs_3Bi_2I_9$ to drive the reduction of CO_2; on the other hand, the photogenerated holes accumulate on CeO_2 to undertake water oxidation. In this case, the assembly of $Cs_3Bi_2I_9$ and CeO_2 nanosheets into Z-scheme heterojunction can significantly promote the separation of photogenerated carriers and enhance the redox capabilities of the photocatalysts simultaneously.

On the basis of clarifying the charge transfer mechanism, we also explore the transfer kinetics of the photogenerated carriers in CeO_2, $Cs_3Bi_2I_9$ and $Cs_3Bi_2I_9/CeO_2$-*x*:1 assembly. First, steady-state photoluminescence (PL) spectra of a series of samples were monitored. As shown in Fig. S19, pure $Cs_3Bi_2I_9$ exhibits a strong characteristic peak at 679 nm. After the introduction of CeO_2, the fluorescence intensity of $Cs_3Bi_2I_9/CeO_2$ is significantly decreased, especially for $Cs_3Bi_2I_9/CeO_2$-3:1 sample, indicating that the assembly of CeO_2 and $Cs_3Bi_2I_9$ can promote the charge transfer at the interface intersection of $Cs_3Bi_2I_9/CeO_2$-*x*:1 assembly. In addition, the charge transfer and separation abilities of CeO_2, $Cs_3Bi_2I_9$ and $Cs_3Bi_2I_9/CeO_2$ were evaluated using photo-assisted Kelvin probe force microscopy (KPFM). As shown in Fig. 5(e), in comparison with CeO_2 and $Cs_3Bi_2I_9$, $Cs_3Bi_2I_9/CeO_2$-3:1 assembly demonstrates the strongest photovoltage response, suggesting that the separation efficiency of the photogenerated electrons and holes in $Cs_3Bi_2I_9/CeO_2$-3:1 are significantly enhanced by the construction of heterojunction. To further investigate the kinetics of photogenerated charge transfer in catalysts, electrochemical impedance spectroscopy (EIS) measurements were performed under light irradiation. As shown in Fig. 5(f), both CeO_2 and $Cs_3Bi_2I_9$ nanosheets have larger arc radius than $Cs_3Bi_2I_9/CeO_2$-3:1 sample, which means CeO_2 and $Cs_3Bi_2I_9$ nanosheets display larger charge transfer resistance than $Cs_3Bi_2I_9/CeO_2$-3:1. Additionally, the time-resolved PL spectra of $Cs_3Bi_2I_9$ and $Cs_3Bi_2I_9/CeO_2$-3:1 (Fig. S20, Table S2) show that, in the presence of CeO_2, the emission lifetime of $Cs_3Bi_2I_9$ decreased from 2.74 to 2.08 ns. These results indicate that $Cs_3Bi_2I_9/CeO_2$-3:1 has the optimal charge transfer efficiency, and the facile electrostatic assembly between $Cs_3Bi_2I_9$ and CeO_2 nanosheets can effectively promote the separation efficiency of the photogenerated charges.

4. Conclusions

In summary, we have developed a facile self-template-oriented method to synthesize 2D lead-free halide perovskite $Cs_3Bi_2I_9$ nanosheets for the first time. Through simple electrostatic self-assembly strategy, $Cs_3Bi_2I_9$ and CeO_2 nanosheets were employed into the construction of a Z-scheme heterojunction as demonstrated by ISI-XPS and ESR measurements. Consequently, the matching energy levels and tight interfacial contact between $Cs_3Bi_2I_9$ and CeO_2 nanosheets can significantly accelerate the charge transfer between $Cs_3Bi_2I_9$ and CeO_2. Furthermore, the environment-friendly halide perovskite composite $Cs_3Bi_2I_9/CeO_2$-3:1 shows outstanding activity for the reduction of CO_2 coupled with the oxidation of H_2O, displaying a record production of 238.21 μmol g^{-1} for CH_4 and CO and a highest electron consumption yield of 877.04 μmol g^{-1} among the reported bismuth-based perovskite photocatalysts. This study enriches the nanostructure of lead-free halide perovskite and boosts their practical applications in the field of artificial photosynthesis.

Declaration of Competing Interest

The authors declare that they have no known competing financial interests or personal relationships that could have appeared to influence the work reported in this paper.

Acknowledgments

This work was financially supported by the Natural Science Foundation of Tianjin City (17JCJQJC43800, 19JCQNJC05500), the National Key R&D Program of China (2017YFA0700104), NSFC (21931007), and the 111 Project of China (D17003).

Appendix A. Supplementary data

Supplementary data to this article can be found online at https://doi.org/10.1016/j.jechem.2022.01.015.

References

[1] C.F. Shih, T. Zhang, J. Li, C. Bai, Joule 2 (2018) 1925–1949.

[2] L. Wang, W. Chen, D.Y. Du Zhang, R. Amal, S. Qiao, J. Wu, Z. Yin, Chem. Soc. Rev. 48 (2019) 5310–5349.

[3] S. Xu, E.A. Carter, Chem. Rev. 119 (2019) 6631–6669.

[4] X. Li, J. Yu, M. Jaroniec, X. Chen, Chem. Rev. 119 (2019) 3962–4179.

[5] Y.-B. Chang, C. Zhang, X.-L. Lu, W. Zhang, T.-B. Lu, Nano Res. 15 (2022) 195–201, https://doi.org/10.1007/s12274-021-3456-2.

[6] A. Mustafa, B.G. Lougou, Y. Shuai, Z. Wang, H. Tan, J. Energy Chem. 49 (2020) 96–123.

[7] Q. Wang, J. Warnan, S. Rodríguez-Jiménez, J.J. Leung, S. Kalathil, V. Andrei, K. Domen, E. Reisner, Nat. Energy 5 (2020) 703–710.

[8] Z.-B. Fang, T.-T. Liu, J. Liu, S. Jin, X.-P. Wu, X.-Q. Gong, K. Wang, Q. Yin, T.-F. Liu, R. Cao, H.-C. Zhou, J. Am. Chem. Soc. 142 (2020) 12515–12523.

[9] S.T. Neatu, J.A. Macia-Agullo, P. Concepcion, H. Garcia, J. Am. Chem. Soc. 136 (2014) 15969–15976.

[10] S. Kreft, R. Schoch, J. Schneidewind, J. Rabeah, E.V. Kondratenko, V.A. Kondratenko, H. Junge, M. Bauer, S. Wohlrab, M. Beller, Chem 5 (2019) 1818–1833.

[11] Y.-F. Xu, M.-Z. Yang, B.-X. Chen, X.-D. Wang, H.-Y. Chen, D.-B. Kuang, C.-Y. Su, J. Am. Chem. Soc. 139 (2017) 5660–5663.

[12] L. Yu, X. Ba, M. Qiu, Y. Li, L. Shuai, W. Zhang, Z. Ren, Y. Yu, Nano Energy 60 (2019) 576–582.

[13] Y. Wang, X. Shang, J. Shen, Z. Zhang, D. Wang, J. Lin, J.C.S. Wu, X. Fu, X. Wang, C. Li, Nat. Commun. 11 (2020) 3043.

[14] J. Wu, X. Li, W. Shi, P. Ling, Y. Sun, X. Jiao, S. Gao, L. Liang, J. Xu, W. Yan, C. Wang, Y. Xie, Angew. Chem., Int. Ed. 57 (2018) 8719–8723.

[15] J.-L. Cheng, Y.-F. Mu, L.-Y. Wu, Z.-L. Liu, K. Su, G.-X. Dong, M. Zhang, T.-B. Lu, Nano Res. (2021), https://doi.org/10.1007/s12274-021-3775-3.

[16] S. Lee, G.Y. Jang, J.K. Kim, J.H. Park, J. Energy Chem. 62 (2021) 11–26.

[17] J. Wang, J. Liu, Z. Du, Z. Li, J. Energy Chem. 54 (2021) 770–785.

[18] X. Zhu, Y. Lin, Y. Sun, M.C. Beard, Y. Yan, J. Am. Chem. Soc. 141 (2019) 733–738.

[19] S. Park, W.J. Chang, C.W. Lee, S. Park, H.-Y. Ahn, K.T. Nam, Nat. Energy 2 (2016) 16185.

[20] J.-F. Liao, Y.-T. Cai, J.-Y. Li, Y. Jiang, X.-D. Wang, H.-Y. Chen, D.-B. Kuang, J. Energy Chem. 53 (2021) 309–315.

[21] X.-K. Liu, W. Xu, S. Bai, Y. Jin, J. Wang, R.H. Friend, F. Gao, Nat. Mater. 20 (2021) 10–21.

[22] Z. Xiao, Z. Song, Y. Yan, Adv. Mater. 31 (2019) 1803792.

[23] J.S. Manser, J.A. Christians, P.V. Kamat, Chem. Rev. 116 (2016) 12956–13008.

[24] L. Liang, P. Gao, Adv. Sci. 5 (2018) 1700331.

[25] Q. Fan, G.V. Biesold-McGee, J. Ma, Q. Xu, S. Pan, J. Peng, Z. Lin, Angew. Chem., Int. Ed. 59 (2020) 1030–1046.

[26] A. Bibi, I. Lee, Y. Nah, O. Allam, H. Kim, L.N. Quan, J. Tang, A. Walsh, S.S. Jang, E. H. Sargent, D.H. Kim, Mater. Today 49 (2021) 123–144, https://doi.org/10.1016/j.mattod.2020.11.026.

[27] Y. Li, Z. Shi, W. Liang, J. Ma, X. Chen, D. Wu, Y. Tian, X. Li, C. Shan, X. Fang, Mater. Horiz. 8 (2021) 1367–1389.

[28] T.C. Jellicoe, J.M. Richter, H.F.J. Glass, M. Tabachnyk, R. Brady, S.E. Dutton, A. Rao, R.H. Friend, D. Credgington, N.C. Greenham, M.L. Böhm, J. Am. Chem. Soc. 138 (2016) 2941–2944.

[29] J. Zhang, Y. Yang, H. Deng, U. Farooq, X. Yang, J. Khan, J. Tang, H. Song, ACS Nano 11 (2017) 9294–9302.

[30] B. Yang, J.S. Chen, F. Hong, X. Mao, K. Zheng, S. Yang, Y. Li, T. Pullerits, W. Deng, K. Han, Angew. Chem., Int. Ed. 56 (2017) 12471–12475.

[31] Y. Tang, C.H. Mak, R. Liu, Z. Wang, L. Ji, H. Song, C. Tan, F. Barrière, H.-Y. Hsu, Adv. Funct. Mater. 30 (2020) 2006919.

[32] T. Wang, D. Yue, X. Li, Y. Zhao, Appl. Catal., B 268 (2020) 118399.

[33] Y. Dai, H. Tüysüz, ChemSusChem 12 (2019) 2587–2592.

[34] Y. Dai, C. Poidevin, C. Ochoa-Hernández, A.A. Auer, H. Tüysüz, Angew. Chem., Int. Ed. 59 (2020) 5788–5796.

[35] B.-M. Bresolin, C. Günnemann, D.W. Bahnemann, M. Sillanpää, Nanomaterials 10 (2020) 763.

[36] J. Sheng, Y. He, J. Li, C. Yuan, H. Huang, S. Wang, Y. Sun, Z. Wang, F. Dong, ACS Nano 14 (2020) 13103–13114.

[37] S.S. Bhosale, A.K. Kharade, E. Jokar, A. Fathi, S.-M. Chang, E.-W.-G. Diau, J. Am. Chem. Soc. 141 (2019) 20434–20442.

[38] Z.-L. Liu, R.-R. Liu, Y.-F. Mu, Y.-X. Feng, G.-X. Dong, M. Zhang, T.-B. Lu, Sol. RRL 5 (2021) 2000691.

[39] B. Ghosh, S. Chakraborty, H. Wei, C. Guet, S. Li, S. Mhaisalkar, N. Mathews, J. Phys. Chem. C 121 (2017) 17062–17067.

[40] B.-M. Bresolin, P. Sgarbossa, D.W. Bahnemann, M. Sillanpää, Sep. Purif. Technol. 251 (2020) 117320.

[41] B.-M. Bresolin, N.O. Balayeva, L.I. Granone, R. Dillert, D.W. Bahnemann, M. Sillanpää, Sol. Energy Mater. Sol. Cells 204 (2020) 110214.

[42] R. Babu, S. Bhandary, D. Chopra, S.P. Singh, Chem. Eur. J. 26 (2020) 10519–10527.

[43] L. Zhou, Y.-F. Xu, B.-X. Chen, D.-B. Kuang, C.-Y. Su, Small 14 (2018) 1703762.

[44] D. Wu, X. Zhao, Y. Huang, J. Lai, J. Yang, C. Tian, P. He, Q. Huang, X. Tang, J. Phys. Chem. C 125 (2021) 18328–18333.

[45] Z. Shi, Z. Cao, X. Sun, Y. Jia, D. Li, L. Cavallo, U. Schwingenschlögl, Small 15 (2019) 1900462.

[46] Q. Han, X. Bai, Z. Man, H. He, L. Li, J. Hu, A. Alsaedi, T. Hayat, Z. Yu, W. Zhang, J. Wang, Y. Zhou, Z. Zou, J. Am. Chem. Soc. 141 (2019) 4209–4213.

[47] Q. Liu, Y. Zhou, J. Kou, X. Chen, Z. Tian, J. Gao, S. Yan, Z. Zou, J. Am. Chem. Soc. 132 (2010) 14385–14387.

[48] L.-Y. Wu, M.-R. Zhang, Y.-X. Feng, W. Zhang, M. Zhang, T.-B. Lu, Sol. RRL 5 (2021) 2100263.

[49] Q. Xu, L. Zhang, J. Yu, S. Wageh, A.A. Al-Ghamdi, M. Jaroniec, Mater. Today 21 (2018) 1042–1063.

[50] J. Bai, J. Sun, X. Zhu, J. Liu, H. Zhang, X.-B. Yin, L. Liu, Small 16 (2020) 1904783.

[51] S. Zhuo, J. Zhang, Y. Shi, Y. Huang, B. Zhang, Angew. Chem., Int. Ed. 54 (2015) 5693–5696.

[52] Z.-W. Wei, H.-J. Wang, C. Zhang, K. Xu, X.-L. Lu, T.-B. Lu, Angew. Chem., Int. Ed. 60 (2021) 16622–16627.

[53] C. Yang, Q. Li, Y. Xia, K. Lv, M. Li, Appl. Surf. Sci. 464 (2019) 388–395.

[54] S. Adhikari, S. Selvaraj, D.-H. Kim, Appl. Catal., B 244 (2019) 11–24.

[55] Y.-F. Mu, W. Zhang, G.-X. Dong, K. Su, M. Zhang, T.-B. Lu, Small 16 (2020) 2002140.

[56] A. Sarkar, P. Acharyya, R. Sasmal, P. Pal, S.S. Agasti, K. Biswas, Inorg. Chem. 57 (2018) 15558–15565.

[57] K. Fan, Y. Jia, Y. Ji, P. Kuang, B. Zhu, X. Liu, J. Yu, ACS Catal. 10 (2020) 358–364.

[58] Z. Jiang, W. Wan, H. Li, S. Yuan, H. Zhao, P.K. Wong, Adv. Mater. 30 (2018) 1706108.